Araya Vargas, J., Meqbel, N., Ritter, O., Brasse, H., Weckmann, U., Yáñez, G., Godoy, B. (2019): Fluid Distribution in the Central Andes Subduction Zone Imaged With Magnetotellurics. - *Journal of Geophysical Research*, *124*, 4, pp. 4017—4034.

DOI: http://doi.org/10.1029/2018JB016933

JGR Solid Earth

RESEARCH ARTICLE
10.1029/2018JB016933

Fluid Distribution in the Central Andes Subduction Zone Imaged With Magnetotellurics

J. Araya Vargas[1,2], N. M. Meqbel[3,4], O. Ritter[4,5], H. Brasse[5], U. Weckmann[4,6], G. Yáñez[1,2,7,8], and B. Godoy[2]

[1]Departamento de Ingeniería Estructural y Geotécnica, Pontificia Universidad Católica de Chile, Santiago, Chile, [2]Centro de Excelencia en Geotermia de los Andes (CEGA), Universidad de Chile, Santiago, Chile, [3]Consulting-GEO, Berlin, Germany, [4]GFZ German Research Centre for Geosciences, Potsdam, Germany, [5]Fachrichtung Geophysik, Freie Universität Berlin, Berlin, Germany, [6]Institute of Earth and Environmental Science, University of Potsdam, Potsdam, Germany, [7]Núcleo Milenio Trazadores de Metales, Universidad de Chile, Santiago, Chile, [8]National Research Center for Integrated Natural Disaster Management (CIGIDEN), Santiago, Chile

Key Points:
- This paper presents a three-dimensional model of the electrical resistivity structure of the Central Andes subduction zone (20°–24°S)
- Resistivity of the mantle wedge suggests along-margin variability in the amount of fluids released by eclogitization of the slab
- Resistivity structure below the arc shows distinctive domains that coincide with segmentation in the distribution of active volcanoes

Supporting Information:
- Supporting Information S1
- Figure S1
- Data Set S1

Correspondence to:
J. Araya Vargas,
jaarayav@ing.puc.cl

Citation:
Araya Vargas, J., Meqbel, N. M., Ritter, O., Brasse, H., Weckmann, U., Yáñez, G., & Godoy, B. (2019). Fluid distribution in the Central Andes subduction zone imaged with magnetotellurics. *Journal of Geophysical Research: Solid Earth*, *124*, 4017–4034. https://doi.org/10.1029/2018JB016933

Received 25 OCT 2018
Accepted 3 MAR 2019
Accepted article online 11 MAR 2019
Published online 4 APR 2019

Abstract We present a model of the electrical resistivity structure of the lithosphere in the Central Andes between 20° and 24°S from 3-D inversion of 56 long-period magnetotelluric sites. Our model shows a complex resistivity structure with significant variability parallel and perpendicular to the trench direction. The continental forearc is characterized mainly by high electrical resistivity (>1,000 Ωm), suggesting overall low volumes of fluids. However, low resistivity zones (LRZs, <5 Ωm) were found in the continental forearc below areas where major trench-parallel faults systems intersect NW-SE transverse faults. Forearc LRZs indicate circulation and accumulation of fluids in highly permeable fault zones. The continental crust along the arc shows three distinctive resistivity domains, which coincide with segmentation in the distribution of volcanoes. The northern domain (20°–20.5°S) is characterized by resistivities >1,000 Ωm and the absence of active volcanism, suggesting the presence of a low-permeability block in the continental crust. The central domain (20.5°–23°S) exhibits a number of LRZs at varying depths, indicating different levels of a magmatic plumbing system. The southern domain (23°–24°S) is characterized by resistivities >1,000 Ωm, suggesting the absence of large magma reservoirs below the volcanic chain at crustal depths. Magma reservoirs located below the base of the crust or in the backarc may fed active volcanism in the southern domain. In the subcontinental mantle, the model exhibits LRZs in the forearc mantle wedge and above clusters of intermediate-depth seismicity, likely related to fluids produced by serpentinization of the mantle and eclogitization of the slab, respectively.

1. Introduction

Fluids play a key role in magmatic, metamorphic, and deformation processes controlling arc volcanism and seismic activity (e.g., Kirby et al., 1996). Study of the fluid distribution in subduction zones can provide, therefore, constrains to better understand the distribution and properties of active volcanism and earthquakes. There is general agreement that dehydration of subducted plates release large amounts of fluids within subduction zones (e.g., Peacock, 1990). However, it is not well constrained where fluids migrate and accumulate after being released from the subducted plate and how the accumulation of these fluids determine the distribution of volcanism (Stern, 2002).

The Andes mountain range is located along the western margin of South America, where orogeny and intense volcanic and seismic activity are attributed to the subduction of oceanic plates beneath the South American plate (e.g., Barazangi & Isacks, 1976; Stern, 2004). The Central Andes at 20°–24°S represents an exceptional natural laboratory to explore how the plate structure and deep fluid distribution are correlated with segmentation of magmatism, because active volcanoes show here a heterogeneous distribution. Remarkably, the volcanic chain exhibits a 175-km gap in recent volcanism (<3 Ma) known as the Pica gap (e.g., Wörner et al., 1992; see red dashed line in Figure 1). In addition, an eastward deflection in the axis of the volcanic chain is observed around the Salar de Atacama basin (see distribution of active volcanoes between 22° and 24.5°S in Figure 1). The segmented distribution of volcanoes along the Central Andes has been attributed to along-margin variability in the composition and permeability of the continental crust (e.g., Götze & Krause, 2002; Wörner et al., 2003). However, along-margin variability in the distribution of

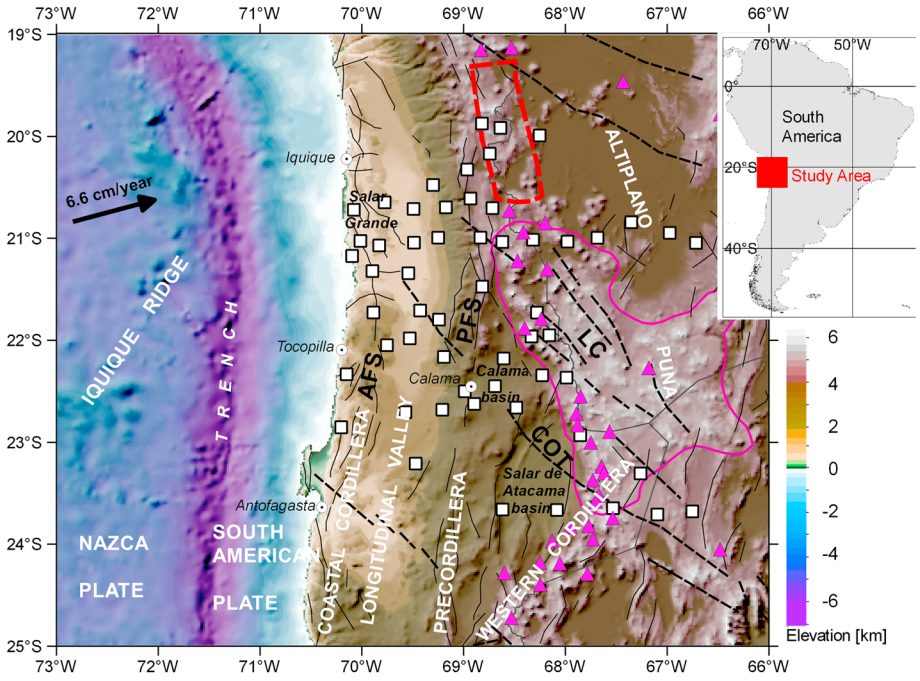

Figure 1. Map of the study area. White squares show locations of the magnetotelluric sites used for this study. Pink triangles indicate active volcanoes (http://volcano.si.edu). Red dashed line outlines the Pica volcanic gap. Pink line outlines the Altiplano-Puna Volcanic Complex (taken from Ward et al., 2014). Black lines indicate major faults (modified from Reutter et al., 1994; Richards et al., 2001; Sernageomin, 2003): AFS = Atacama Fault System; PFS = Precordilleran Fault System. Black dashed lines are NW-SE transverse fault systems (taken from Richards et al., 2001; Tibaldi et al., 2009): COT = Calama-Olacapato-El Toro; LC = Lípez-Coranzuli. Elevation data are obtained from ETOPO1 Global relief model (www.ngdc.noaa.gov/mgg/global/global.html).

fluids and partial melts feeding the volcanic arc has not been fully addressed, although there is a number of seismological, seismic, magnetotelluric (MT), gravimetric, and heat flow studies that have constrained the lithospheric-scale structure of the subduction zone at some segments of this region (see, e.g., ANCORP working group, 2003). Most of the previous geophysical studies have been conducted either along profiles perpendicular to the margin direction separated by several hundred kilometers (e.g., Brasse et al., 2002; Yuan et al., 2000) or with arrays concentrating in the forearc (e.g., Sippl et al., 2018) or in the arc/backarc domains (e.g., Schurr et al., 2003; Ward et al., 2014).

The electrical resistivity of rocks is a physical property that is highly sensitive to the presence of interconnected fluids or partial melts (Unsworth & Rondenay, 2013). Images of the electrical resistivity structure have been widely used to estimate the distribution of fluids in subduction zones (Worzewski et al., 2011). In this paper, we study the deep electrical resistivity structure of the Central Andes to estimate the fluid distribution within the subduction zone. We present an electrical resistivity model derived from 3-D inversion of MT data collected at an array of stations distributed between 20° and 24°S. Based on the correlation of our model with independent geological and geophysical information, we identify regions of the subduction zone where fluids and partial melts are concentrated. We show that the distribution of these fluid and magma reservoirs seem to control the distribution of the volcanic arc.

2. Tectonic Setting

The oceanic Nazca Plate subducts beneath the continental South American Plate along the Central Andes with a convergence rate of 6.6 cm/year and an azimuth of 78° (Angermann et al., 1999). In the study area, the Nazca plate is characterized by subduction angles between 25° and 30° (e.g., Barazangi & Isacks, 1976), the oldest segment of oceanic crust at the trench of the western margin of South America (50 Myr, Müller et al., 1997), and the subduction of a seamount chain (the Iquique ridge, e.g., Contreras-Reyes & Carrizo, 2011; see Figure 1). Five major longitudinal morphological units are observed in the study area from west to east (see Figure 1): the

Coastal Cordillera, the Longitudinal Valley, the Chilean Precordillera, the Western Cordillera, and the Altiplano-Puna region. The geology of the study area is dominated by outcrops of rocks of post Triassic age, related to the evolution of the subduction zone along the western margin of South America. The distribution of intrusive rocks suggests that the axis of the magmatic arc have progressively migrated from west to east since the Jurassic (e.g., Coira et al., 1982). The active volcanic arc is located at the Western Cordillera.

The Coastal Cordillera is a 1- to 2-km-high and 20- to 50-km-wide mountain range. Its geology is dominated by outcrops of volcanic and plutonic rocks of Jurassic to Early Cretaceous age, partly covered by Cenozoic unconsolidated continental sediments. The Longitudinal Valley is a relatively flat basin, mainly filled with Cenozoic continental sediments and ignimbrites. The Precordillera is a 2- to 4-km-high mountain range, with outcrops of Paleozoic, Mesozoic, and Cenozoic rocks. Two large basins separate the Precordillera from the Western Cordillera between 22° and 24°S (Calama and Salar de Atacama basins in Figure 1), which are mainly filled by Cenozoic sedimentary deposits (e.g., Jordan et al., 2010).

The Western Cordillera is a mountain range with average altitude of 3–4 km, with volcanic edifices reaching up to 6-km height. Rocks and deposits derived from Quaternary volcanism dominate the geology of this region. More than 20 active volcanoes and potentially active ignimbrite centers have been documented along the Western Cordillera in the study area (Stern, 2004; pink triangles indicate active volcanoes in Figure 1). The Altiplano-Puna region is a ~300-km-wide plateau with an average elevation of 3.8 km, where mostly Cenozoic sediments and volcanic deposits are observed. A large area of the Altiplano-Puna is covered with Neogene ignimbrites (the Altiplano-Puna Volcanic Complex, APVC, pink line in Figure 1), which are thought to be a consequence of large-scale crustal melting (de Silva, 1989). Geophysical studies have imaged zones of low seismic velocity and low electrical resistivity below the APVC (e.g., Brasse et al., 2002; Chmielowski et al., 1999; Comeau et al., 2015; Pritchard et al., 2018; Ward et al., 2014), suggesting the presence of a large-scale magma reservoir (the Altiplano-Puna Magma Body).

The active volcanic chain in the study area can be divided in three major domains. The “Pica Gap” extends from 19°10′ to 20°44′S (Wörner et al., 1992, see Figure 1) and corresponds to a segment on which volcanic activity is absent since Middle Pleistocene (Gardeweg & Sellés, 2017; Wörner et al., 2000). Volcanism between 21° and 24°S is mainly related to partial melting of the mantle and later crustal contamination of mantle-derived material (up to 50:50% vol.) at lower and middle crustal levels (de Silva & Kay, 2018). Processes of assimilation-fractional crystallization (de Paolo, 1981) related to the presence of the AMPB have been interpreted in middle levels of the continental crust (Burns et al., 2015; Godoy et al., 2014, 2017). At ~24°S, depletion on heavy rare Earth element concentrations suggests a major involvement of the lower crust (i.e., garnet fractionation), indicating that assimilation-fractional crystallization-type processes occur mainly at the mantle-crust boundary, with a minor involvement of contamination at upper crustal levels (e.g., Coira & Kay, 1993; Matteini et al., 2002).

Two major trench-parallel fault systems are recognized in the study area: the Atacama and the Precordilleran Fault Systems (AFS and PFS in Figure 1, respectively). The AFS can be traced for more than 1,000 km along the Coastal Cordillera and cuts Mesozoic rocks and Cenozoic sediments. Kinematic studies of the AFS suggest predominantly left-lateral strike-slip and normal movements during Jurassic to Early Cretaceous, and reactivation of faults with normal and reverse displacements during the Cenozoic (e.g., Allmendinger & González, 2010). The PFS has been described between 19° and 27°S along the Precordillera. Dextral and sinistral strike-slip displacements and reverse movements are documented for the PFS (e.g., Amilibia et al., 2008). Second-order NW-SE transverse fault systems have been identified from regional alignment of faults and morphological lineaments (Calama-Olacapato-El Toro [COT] and Lípez-Coranzuli [LC] in Figure 1). It has been suggested that transverse faults systems represent boundaries of pre-Andean basement blocks, whose reactivation during the Andean tectonic cycle has partially controlled the distribution of basins, volcanoes, calderas, and dikes (e.g., Salfity, 1985).

3. Methods

3.1. MT Data

Magnetotellurics is a geophysical method to image the electrical resistivity distribution of Earth's subsurface structure, which is estimated from measurements of naturally occurring electric and magnetic field

variations at the ground surface (see e.g., Chave & Jones, 2012). Following MT theory, the mathematical relationship between measured electric and magnetic fields is described in the frequency domain by parameters called *transfer functions* (TFs):

$$\boldsymbol{E}_h = \underline{\boldsymbol{Z}}\boldsymbol{B}_h,$$

$$\boldsymbol{B}_z = \boldsymbol{T}\boldsymbol{B}_h,$$

where all quantities depend on period (s; reciprocal of frequency); $\boldsymbol{E}_h$ and $\boldsymbol{B}_h$ are the horizontal electric and magnetic field components, respectively; $\underline{\boldsymbol{Z}}$ is the 2×2 complex impedance tensor; $\boldsymbol{B}_z$ is the vertical magnetic field component; and $\boldsymbol{T}$ is a nondimensional 1×2 complex vector called the vertical magnetic TF (VTF, sometimes referred in the literature as *tipper*). VTFs are diagnostic of lateral resistivity contrasts and are typically presented as induction vectors. In map view, the lengths and directions of the induction vectors depend on the size and geometry of resistivity contrasts. In the Wiese (1962) convention, the induction vectors calculated from the real parts of $\boldsymbol{T}$ tend to point away from the low resistive side of a resistivity contrast. Usually, elements of the impedance tensor $\underline{\boldsymbol{Z}}$ are displayed as apparent resistivity (ρ_a [Ωm]) and phase (ϕ [degrees]):

$$\rho_{a,ij} = \frac{1}{\mu_0 \omega} \left\| Z_{\boldsymbol{ij}} \right\|^2,$$

$$\phi_{ij} = \arctan\left(\frac{\mathrm{Imag}\{Z_{\boldsymbol{ij}}\}}{\mathrm{Real}\{Z_{\boldsymbol{ij}}\}} \right),$$

where i and j are the two horizontal directions along which electromagnetic fields are measured in the field; Z_{ij} are components of $\underline{\boldsymbol{Z}}$; μ_0 is the magnetic permeability of free space (1.2566×10^{-6} [H/m]); and $\omega = 2\pi$ per period. Some components of measured electric fields can be affected by a phenomenon called *galvanic distortion*, which difficult the interpretation of $\underline{\boldsymbol{Z}}$. An alternative representation of $\underline{\boldsymbol{Z}}$ is the nondimensional phase tensor $\underline{\boldsymbol{\Phi}}$:

$$\underline{\boldsymbol{\Phi}} = \mathrm{Real}\,(\underline{\boldsymbol{Z}})^{-1}\mathrm{Imag}\,(\underline{\boldsymbol{Z}}).$$

Unlike $\underline{\boldsymbol{Z}}$, the phase tensor is not affected by galvanic distortion (Caldwell et al., 2004). The phase tensor is characterized by rotational invariants, whose properties can give information about the dimensionality of the resistivity structure (Caldwell et al., 2004). It can be shown that the phase tensor skew angle $\boldsymbol{\beta}$ is 0 in 1-D and 2-D environments.

$$\boldsymbol{\beta} = \mathbf{0.5}\ \arctan\left(\frac{\boldsymbol{\Phi_{xy}} - \boldsymbol{\Phi_{yx}}}{\boldsymbol{\Phi_{xx}} + \boldsymbol{\Phi_{yy}}} \right)$$

To obtain a model of the lithospheric-scale electrical resistivity structure of the study area, we compiled a data set comprising field experiments carried out in northern Chile, southern Bolivia and northern Argentina since 1980s (see Table S1 in the supporting information). In all these studies, magnetic field variations were measured using three-component fluxgates magnetometers, while the horizontal components of the electric field were measured with nonpolarizing electrodes. At all MT stations, the instruments were oriented using a geomagnetic coordinate system. All TFs in these studies were calculated using robust processing codes (see Table S1). The compiled sites are not uniformly distributed in the study area. To avoid spatial bias in the characterization of the resistivity structure, we selected to invert 56 out of 157 available sites. The selected 56 sites define a semiregular mesh following an average site spacing of 50 km. A few stations had to be discarded due to low data quality. The selected data set comprises estimates of all TFs at 24 periods equally spaced in logarithmic scale between 10 and ~10,000 s, obtained after interpolating the original data using linear spline with the 3-D Grid academic software (www.consulting-geo.com). At 14 sites TFs were available only for periods between 100 and 3,000 s (see supporting information).

Some regional patterns can be identified in TFs of the selected data set. Figure 2 shows phase tensor ellipses and induction vectors for all sites at four exemplary periods. The phase tensor ellipses in Figure 2 are drawn from the phase tensor $\underline{\boldsymbol{\Phi}}$ following Caldwell et al. (2004) and colored with the associated value of phase

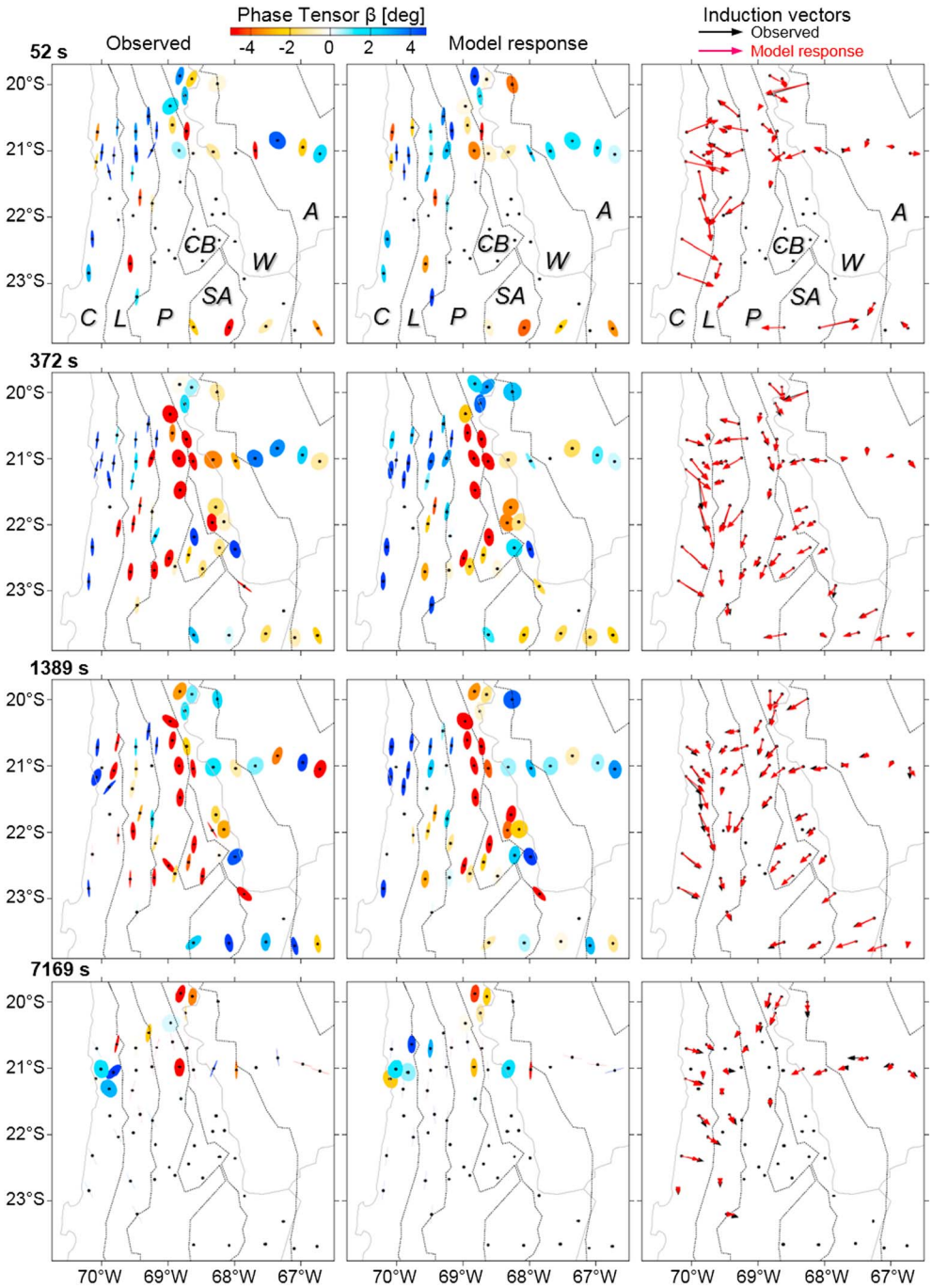

Figure 2. Overview of the data at four exemplary periods (along rows). The left and center columns show the phase tensor ellipses calculated from the data (left) and from the preferred model responses (center). Each ellipsis is colored according to the phase tensor β parameter. The right column shows induction vectors calculated from the data (black) and from the preferred model responses (red). Black lines are limits of major geomorphological units: *A* = Altiplano-Puna; *C* = Coastal Cordillera; *CB* = Calama basin; *L* = Longitudinal Valley; *P* = Precordillera; *SA* = Salar de Atacama; *W* = Western Cordillera.

tensor β. Most sites show $|\beta| > 0°$ (Figure 2, left column), suggesting that the resistivity structure is 3-D. Induction vectors point away from the coast at sites in the Coastal Cordillera (Figure 2, right column), pattern which it is expected due to the very low resistivity of the ocean (e.g., 0.3 Ωm reported in Kapinos et al., 2016). It is not intuitive, however, to see that at most sites of the Coastal Cordillera, Longitudinal Valley, and Precordillera that induction vectors are deflected to the south. Such pattern has been observed before and

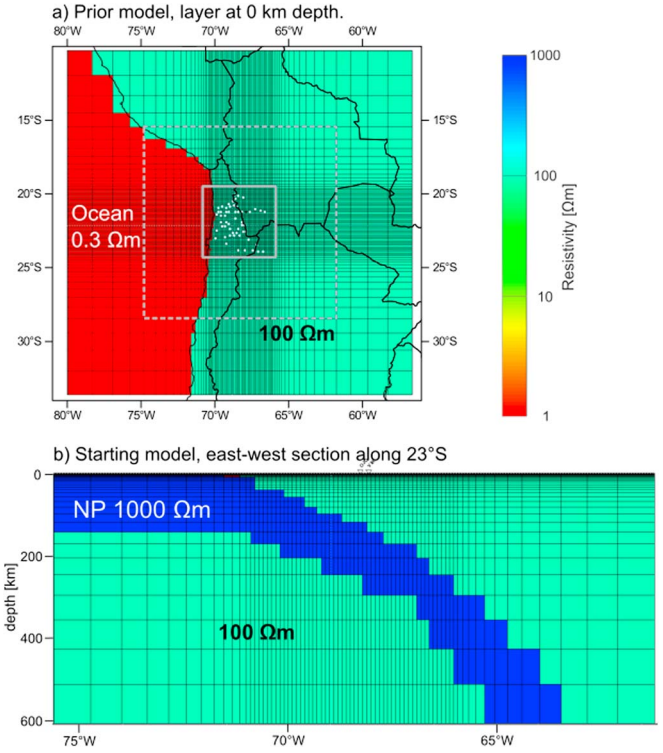

Figure 3. Setup of the 3-D inversion modeling. (a) Prior model, layer between 0- and 0.05-km depth. The dotted-line and solid-line gray rectangles indicate the area of nested model and model core, respectively. White dots show locations of the magnetotelluric sites. Black lines show coastline and country borders for reference. (b) Starting model for nested inversion, section at 23°S. NP = a priori structure simulating the downgoing Nazca plate.

explained by a combination of 3-D features and large-scale electrical anisotropy (e.g., Kühn et al., 2014). At sites in the Longitudinal Valley, Precordillera, and Western Cordillera induction vectors point westwards, suggesting a low resistivity zone (LRZ) east of the Western Cordillera, likely related to the Bolivian Altiplano anomaly described by a number of studies (e.g., Brasse et al., 2002).

3.2. Modeling of Electrical Resistivity

To explain the observed MT data, we modeled the data with the 3-D inversion program ModEM (Egbert & Kelbert, 2012; Kelbert et al., 2014), parallelized using the scheme of Meqbel (2009). We used a version of ModEM that applies the finite differences method to solve Maxwell's equations numerically and a nonlinear conjugate gradients algorithm to solve the minimization problem of the inversion process. To find a resistivity model ($\mathbf{m}$) that can explain the data ($\mathbf{d}$, i.e., $\underline{\boldsymbol{Z}}$ and $\boldsymbol{T}$), ModEM minimizes an objective function ($\boldsymbol{\Psi}$) with respect to the model parameters (the resistivity of the cells which form the model). The objective function $\boldsymbol{\Psi}$ comprises two terms (see equation (1)): a measure of the data misfit (disagreement between measured data and model responses) and a regularization term. The regularization term is added to stabilize the inversion process and to generate models that favor coherent resistivity structures between adjacent cells.

$$\Psi(\mathbf{m},\mathbf{d}) = \underbrace{(\mathbf{d}-\mathbf{f}(\mathbf{m}))^T\mathbf{C}_\mathbf{d}^{-1}(\mathbf{d}-\mathbf{f}(\mathbf{m}))}_{\text{data misfit term}} + \underbrace{\lambda(\mathbf{m}-\mathbf{m}_0)^T\mathbf{C}_\mathbf{m}^{-1}(\mathbf{m}-\mathbf{m}_0)}_{\text{regularization term}} \quad (1)$$

In equation (1), $f(\mathbf{m})$ is the forward response of model $\mathbf{m}$, $\mathbf{C_d}$ is the covariance of data errors, λ is a trade-off parameter that controls the contribution of the regularization term to the objective function, $\mathbf{m}_0$ is the prior model, and $\mathbf{C_m}$ is the model covariance. The covariance matrix $\mathbf{C_d}$ contains the inverse of the squared data errors; therefore, calculation of misfit and how the inversion process evolves depends greatly on the magnitude of the data errors. After testing various options, we did not use statistically determined data errors but error bounds as this resulted in better overall fit of all TFs components. For all components of $\boldsymbol{T}$ fixed error bounds of 0.03 were used. In the case of $\underline{\boldsymbol{Z}}$, the errors assigned to each component were calculated as a percentage of the product of off-diagonal components of $\underline{\boldsymbol{Z}}$ (Z_{xy} and Z_{yx}). After trying several combinations, an acceptable global misfit and better fit of all components was obtained by setting: $Z_{xx} = Z_{yy} = 20\%$ of $(Z_{xy}{\cdot}Z_{yx})^{1/2}$ and $Z_{xy} = Z_{yx} = 10\%$ of $(Z_{xy}{\cdot}Z_{yx})^{1/2}$. Although this error setup apparently down weights diagonal components of $\underline{\boldsymbol{Z}}$ (Z_{xx} and Z_{yy}), in practice it resulted in a better fit of all components. The regularization term in equation (1) forces the inversion to obtain models that are (i) smooth and (ii) as close as possible to the prior model $\mathbf{m}_0$ but still fitting the data. The model covariance matrix $\mathbf{C_m}$ partly depends on the parameter α (not shown in equation (1)), which controls model smoothness in each coordinate direction. The larger the values of α, the smoother is the resulting inversion model. After testing a range of values for α (between 0.01 and 1), and evaluating the related inversion results, we finally chose an intermediate value of $\alpha = 0.2$, because it resulted in smooth but still geologically meaningful, resistivity models. This smoothing factor was applied uniformly in all spatial directions.

Our model domain consists of a volume of 2,780 km × 2,780 km × 4,194 km in the x, y, and z directions, divided in 82 × 82 horizontal cells and 51 vertical layers, respectively (Figure 3a). In the core of the model, which is defined by an area of 500 km × 500 km centered at 22°S and 69°W, cells have horizontal dimensions of 10 km. In the outer parts of the model, horizontal sizes of the cells increase by a factor of 1.2 with increasing distance from the core. Layer thicknesses start with 50 m at surface and then increase by a factor of 1.2 with depth. Topography was not considered. Our prior or reference model ($\mathbf{m}_0$ in equation (1)) consists of a homogenous half space of 100 Ωm and a 0.3-Ωm 3-D body simulating the ocean

(Figure 3a). The geometry of the ocean body was constrained using 1 arc-minute resolution bathymetry data from National Oceanic and Atmospheric Administration (www.ngdc.noaa.gov/mgg/topo/topo.html). In all tests, we fixed the shape and resistivity of the ocean body in the prior model. After performing a number of tests, we observed that the inversion systematically created cells with very high resistivity along the coastline and beneath the continental shelf. Likely, our model of the ocean conductance (i.e., the ratio between ocean thickness and its resistivity) was overestimating the real one, especially because the minimum cell size in our model is too coarse to reproduce accurately the thickness of the ocean close to the coast. The inversion tried to compensate this excess of conductance by creating unrealistically high resistivities in cells closest to the fixed ocean body. We therefore used a prior model where coastline and continental shelf were positioned two or three cells further offshore of their actual position. Effectively, the inversion used these extra cells to create a smoother land-ocean transition. To reduce the overall computation time required for the inversion processes, we used a nested modeling approach (see, e.g., Meqbel et al., 2014). The nested model subspace covers an area of 1,560 km × 1,450 km centered on the array of stations (Figure 3a).

ModEM can use a starting model, in addition to a prior model, to compute the initial misfit term (equation (1)) and which then represents a "first guess" to initiate the inversion process. Features in the starting model are not fixed, and their shape and resistivity can evolve during the inversion process. Our starting model (Figure 3b) comprises a homogenous half space of 100 Ωm and two additional features: (i) a bathymetry-constrained 0.3-Ωm body representing the ocean and (ii) a 1,000-Ωm body mimicking the geometry of the Nazca lithosphere (labeled NP in Figure 3b). Contrary to the prior model (see above), we did not modify the bathymetry-constrained ocean body in the starting model. Inclusion of a more realistic model of the ocean in the starting model significantly improved the fit of the data at coastal sites but without causing artifacts due to an overestimated ocean conductance as described above. Previous MT studies from other subduction zones indicated that more realistic resistivity models can be obtained if the oceanic slab is included as a priori information (e.g., McGary et al., 2014). We assumed an average thickness of 80 km for the oceanic Nazca plate. The upper limit was constrained by using the geometry of the Slab 1.0 model (Hayes et al., 2012). Marine MT studies suggest that oceanic lithosphere is characterized by resistivities >1,000 Ωm (e.g., Worzewski et al., 2011). Inclusion of the a priori NP resistor in the starting model improved the overall data fit and resulted in resistivity structure of the forearc mantle that is better correlated with models derived from seismic studies (see section 5).

4. Results

The preferred model was obtained after 97 iterations, in which the global root-mean-square misfit value (computed over all sites, periods, and TFs) was reduced from 15.78 to a value of 1.37. Figure 2 shows observed TFs and the respective responses of our preferred 3-D resistivity model at four representative periods. Curves obtained for all sites are shown in the supporting information. The overall data fit is good; the model responses reproduce all major trends in the observations, over the entire period range and for all components of the measured data. The model reproduces quite well the shape and orientation of phase tensor ellipses (compare left and center columns of Figure 2), and the magnitude and azimuth of induction vectors (even the very large vectors observed at coastal sites, see right column in Figure 2).

Figure 4 shows horizontal slices of our preferred model at four different depths. Pale colors represent areas where low resolution of the model was estimated (see Resolution Tests in the supporting information). The model shows a number of low resistivity zones (LRZs) that together yield a complex 3-D structure. Aside of the ocean, the major structure obtained in the study area is a domain of high resistivity (>1,000 Ωm) observed along the forearc, the forearc high resistivity zone (FHRZ in Figures 4a–4c). The FHRZ body is observable at least from 5-km depth to the top of the a priori body simulating the Nazca plate (body NP in Figure 3b); for deeper levels, it is not possible to differentiate between these two high resistivity features. Furthermore, the model shows a number of additional distinct and large-scale LRZs (most of them <5 Ωm) that have important implications for the main purpose of this study. We labeled these features following the morphological region below which they are located. We conducted a series of additional inversion and forward modeling tests to evaluate the robustness of all LRZs that are described in the next paragraphs (see Sensitivity Tests in the supporting information).

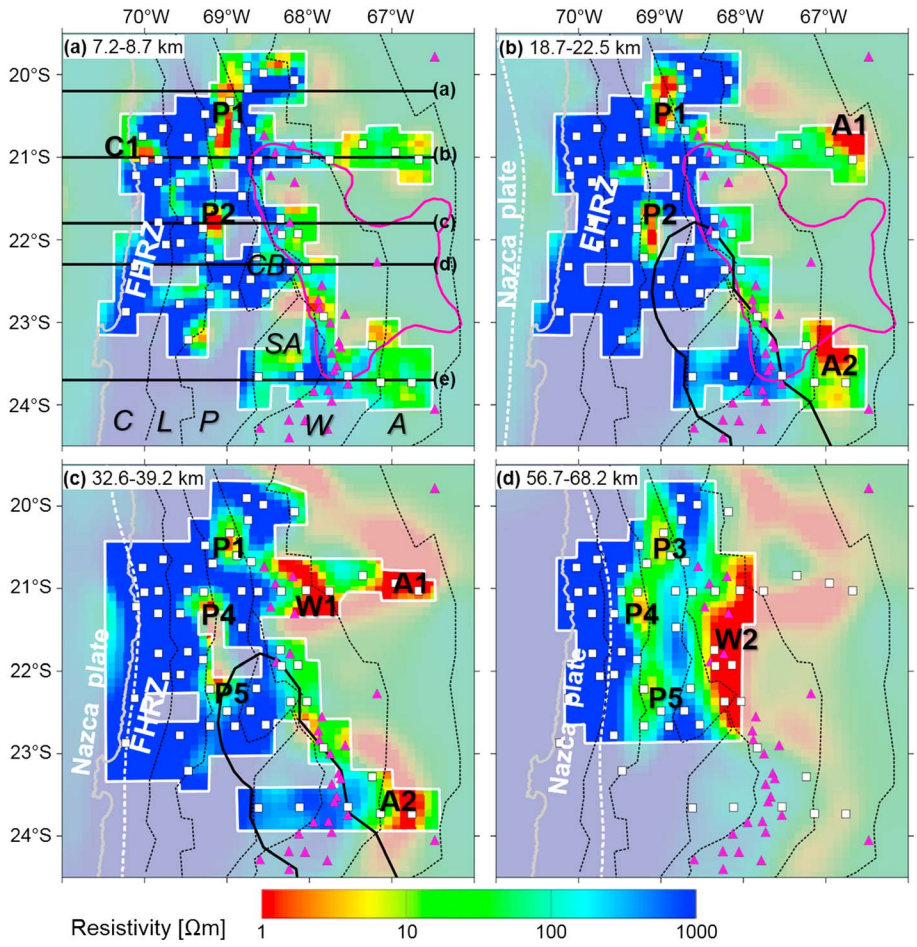

Figure 4. Selected horizontal layers of the preferred resistivity model. Pale colors are regions of low model resolution (see Resolution Tests in the supporting information). White squares are magnetotelluric sites. Pink triangles are active volcanoes. Gray thin line indicates the coastline. Black thin lines are limits of major geomorphological units: *A* = Altiplano-Puna; *C* = Coastal Cordillera; *CB* = Calama basin; *L* = Longitudinal Valley; *P* = Precordillera; *SA* = Salar de Atacama; *W* = Western Cordillera. Black thick lines in (a) indicate location of sections shown in Figure 5. Pink line in (a) and (b) outlines the Altiplano-Puna Volcanic Complex (taken from Ward et al., 2014). White dotted lines in (b) and (d) indicate the eastern boundary of the subducted Nazca plate at 20-, 40-, and 60-km depths, respectively (taken from Hayes et al., 2012). Major resistivity features discussed in the text are labeled with letters followed by a number, except forearc high resistivity zone (FHRZ).

Our preferred model shows only one LRZ below the Coastal Cordillera (C1) in the Salar Grande area (centered at ~21°S, 70°W; Figure 4a). C1 is located in the upper crust (at 4- to 9-km depth, Figure 5b) and shows a horizontal extent of 20 × 20 km^2. C1 has strong influence on TFs at surrounding sites (see Test 1 in the supporting information), suggesting that it is well constrained by the data. However, the western boundary of this anomaly may be not well resolved due to lack of sites along the coast. C1 roughly coincides with LRZs found by Lezaeta (2001) and Kühn et al. (2014) in the same area at similar depths.

Below the Precordillera and Longitudinal Valley-Precordillera boundary we identified two LRZs at upper to middle crustal depths (P1 and P2, Figures 4a–4c and 5a–5c), and three LRZs extending between the lower crust and mantle (P3–P5, Figures 4c and 4d, 5a and 5b, and 5c). Although the center of each of these anomalies define distinctive LRZs, they seem to be partially connected at some areas of the model (P1 with P3 and P4, and P2 with P4 and P5). P1 and P3 extend along 69°W between ~20° and 21°S. The east-west extent of these anomalies is well constrained by the data, but their northern boundary may be not well resolved due to lack of stations north of 20°S. P1 appears approximately at the same location and vertical extent but larger in size, as the Precordilleran conductor modeled in the upper crust by Soyer and Brasse (2001), Brasse et al. (2002), and Kühn et al. (2014). P2, P4, and P5 are located between 21° and 22.5°S, a segment

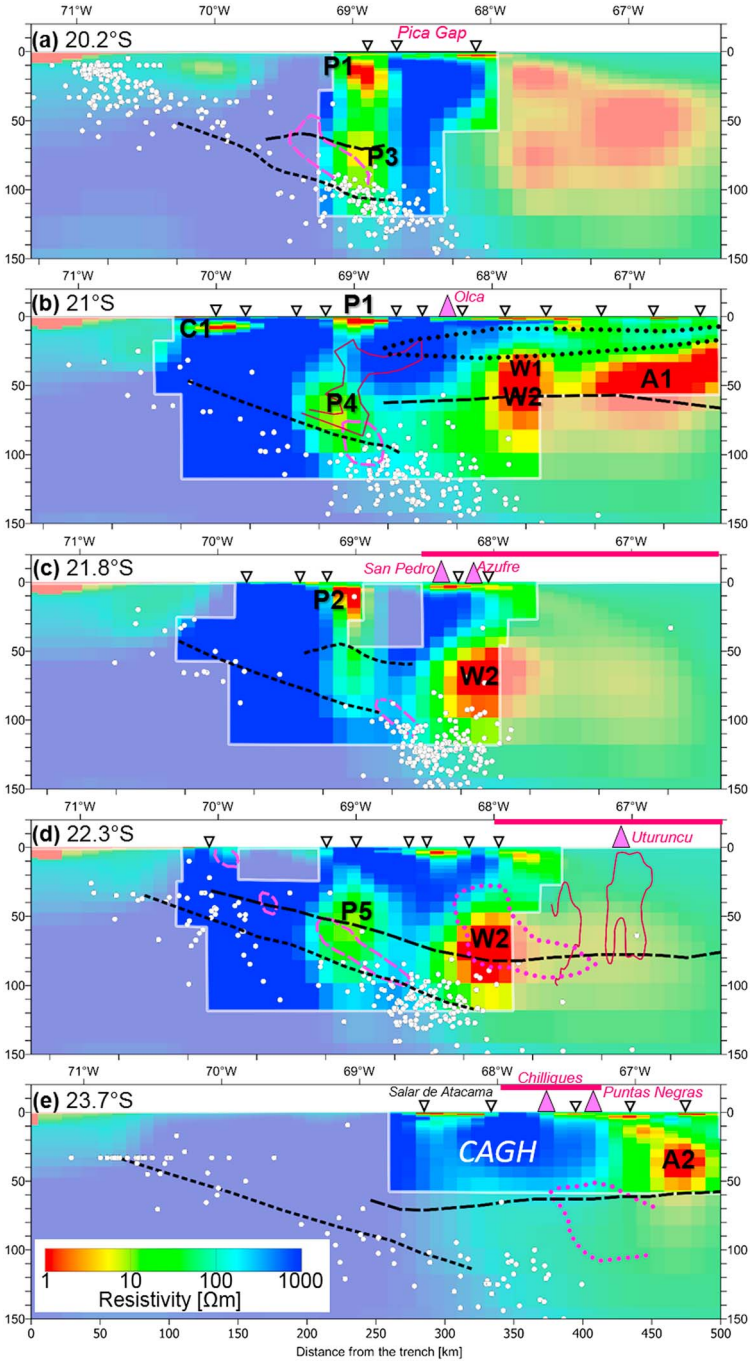

Figure 5. Comparison between sections through the preferred resistivity model and independent geological and geophysical information. Pink triangles and white inverted triangles on top of the sections are active volcanoes and magnetotelluric sites within 30 km of the displayed sections, respectively. White dots are hypocenters located within 20 km of the displayed sections, obtained from the U.S. Geological Survey catalogue (see the text). Black dashed lines in (a)–(e) are the continental Moho and slab top reflectors shown in Sodoudi et al. (2011) at 20°S, ANCORP (2003) at 21°S, Sodoudi et al. (2011) at 22°S, Yuan et al. (2000) at 22.4°S, and Yuan et al. (2000) at 23.4°S, respectively. Pink dashed lines in (a)–(d) encloses zones of *P*-wave to *S*-wave ratio (*Vp*/*Vs*) larger than 1.77 shown in Comte et al. (2016) at ~20.4°, 21°, 21.9°, and 22.4°S, respectively. Black dotted lines in (b) indicate the top and bottom of the Altiplano low velocity zone (taken from ANCORP, 2003). Dark pink line in (b) encloses high seismic reflectivity zone interpreted by Yoon et al. (2009). Pink dotted contour in (d, e) encloses zones of high attenuation in *P*-wave velocity ($Qp \leq 200$) shown in Schurr et al. (2003) at 22.1° and 23.5°S, respectively. Dark pink continuous line in (d) encloses zones of $Vp/Vs > 1.8$ shown in Kukarina et al. (2017) at ~22.3°S below the Altiplano region. Thick pink lines on top of (c)–(e) indicate projection along those section of the area interpreted for the Altiplano-Puna Volcanic Complex (since Ward et al., 2014). CAGH = Central Andean gravity high.

of the Precordillera and Longitudinal Valley with sparse site coverage and low model resolution (see pale regions of the model at 22°S/69°W in Figures 4a–4c). The western boundary of these anomalies seems to be constrained by the data (see Sensitivity Tests 3, 5, and 6 in the supporting information), but their eastern boundary may be not well resolved due to lack of stations. Although we estimate low model resolution in the forearc south of 22.7°S, additional forward and inversion modeling tests suggest that the overall resistivity of the lower crust/forearc mantle below the Precordillera is relatively higher between 23.5° and 24.5°S, and it is likely that LRZs comparable in size and resistivity with P3, P4, and P5 are absent along this segment (see Sensitivity Tests 7 and 8 in the supporting information).

Along the Western Cordillera the model shows two LRZs (W1 and W2) that seem to be connected below 50-km depth (Figure 5b). W1 is found in the Western Cordillera-Altiplano boundary at 21°S (Figures 4c–4d), at depths ranging between 20 and ~50 km (Figure 5b). The extent of this LRZ is constrained in east-west direction by the data (see Sensitivity Tests 9, 11, and 15 in the supporting information), but our data set has not site coverage to resolve the northern and southern boundaries of this anomaly. W2 lies along the Western Cordillera between ~20.5° and 22.7°S (Figure 4d), at 47- to 98-km depth (Figures 5b–5d). Sensitivity tests suggest that the northern and western boundaries of W2 are well constrained by the data (see Test 10 in the supporting information). The eastern and southern boundaries of W2 may be not well resolved due to lack of stations in this part of the model (see Figure 4d). However, additional inversion tests suggest that W2 does not extend below the Altiplano nor the volcanic chain south of 23°S (see Tests 12 and 15 in the supporting information).

Our preferred model shows two LRZs (A1 and A2) below the Altiplano-Puna region approximately at 67°W (Figures 4b and 4c). A1 is observed at 21°S between 20- and ~70-km depths (Figure 5b). Sensitivity tests suggest that A1 is strongly required by the data, but the north-south extent of this anomaly may be not well resolved due to lack of sites (see Tests 13 and 15 in the supporting information). The region occupied by A1, W1, and W2 along 21°S roughly coincides with the Bolivian Altiplano conductor shown in Brasse et al. (2002) and Kühn et al. (2014). A2 is centered at 23.7°S and extends between 20- and ~60-km depths (Figure 5e). Sensitivity tests suggest that the western boundary of this anomaly is constrained by the data, but its eastern boundary may be not well resolved due to lack of sites in the Puna region (see Tests 14 and 15 in the supporting information). A2 spatially coincides with the conductor *D* showed in Díaz et al. (2012).

Although MT is mostly sensitive to structures of low resistivity, we deduce that east-west extent of the FHRZ is well defined because this body is sandwiched between low resistivity structures (e.g., C1 and P1 in Figure 4a). Furthermore, structures with similar characteristics to the FHRZ were found in other MT studies from different segments of the northern Chile forearc (Brasse et al., 2002; Brasse & Eydam, 2008; Díaz et al., 2012; Lezaeta, 2001).

5. Discussion

There are remarkable spatial correlations between main resistivity features of our preferred model and major lithospheric structures described by independent geological and geophysical studies. Figure 5 shows sections of our resistivity model in comparison with independent geophysical data. For reference the figures show locations of earthquakes with magnitude >2.5, registered between 1 January 1973 and 17 January 2018, downloaded from the catalogue of the U.S. Geological Survey (https://earthquake.usgs.gov/earthquakes/search/). Most of the major LRZs revealed in our model coincide with regions where seismological and seismic studies suggest the presence of large-scale (>1,000 km^3) fluid reservoirs.

5.1. Continental Forearc Structure

The resistivity structure of the continental plate forearc between the coast and the Precordillera is dominated by resistivities >1,000 Ωm (the FHRZ), aside the presence of some LRZs (see next paragraph). The east-west extent of the FHRZ coincides with a domain of the forearc characterized by higher density (Schaller et al., 2015), higher *P*- and *S*-wave velocities (Koulakov et al., 2006), and lower seismic attenuation (Schurr et al., 2003) in comparison to the Precordillera. Based on seismic properties of the western forearc and complemented with thermal models of the subduction zone (Springer, 1999), it was suggested that this region embodies a rigid and cold block (e.g., Schurr et al., 2003). Taking into account the high resistivities (>1,000 Ωm) dominating the FHRZ, we deduce that this structure represents a segment of the forearc

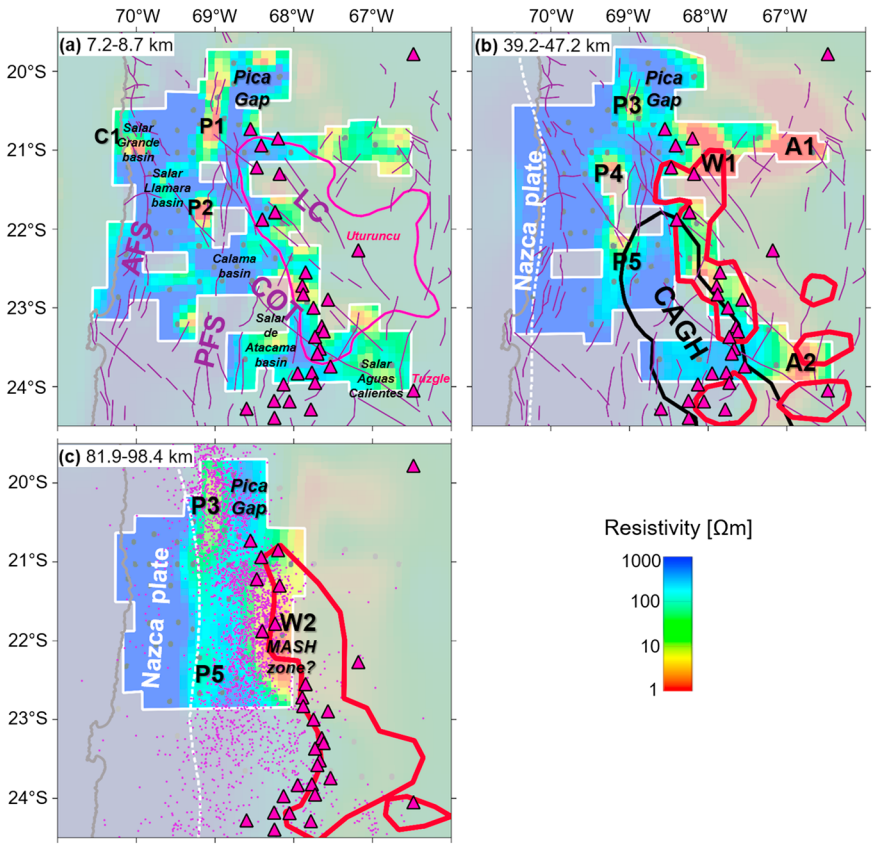

Figure 6. Preferred resistivity model layers at (a) 7.2- to 8.7-km, (b) 39.2- to 47.2-km, and (c) 81.9- to 98.4-km depths showing interpretation of major resistivity features. Pink triangles are active volcanoes. Gray line indicates the coastline. Pink line in (a) outlines the Altiplano-Puna Volcanic Complex (taken from Ward et al., 2014). Purple lines in (a, b) are major faults and regional structural lineaments. Black line in (b) encloses the location of the CAGH gravity anomaly (taken from Götze & Krause, 2002). Red line in (b) and (c) encloses zones of high attenuation in *P*-wave velocity ($Qp \leq 200$) shown in Schurr et al. (2003) at 40- and 85-km depths, respectively. White line in (b) and (c) indicates the eastern boundary of the slab at 40- and 80-km depths, respectively (taken from Hayes et al., 2012). Purple dots in (c) are epicenters from seismic events located at 80- to 150-km depth. CAGH = Central Andean gravity high; PFS = Precordilleran Fault System; AFS = Atacama Fault System; MASH = Melting, Assimilation, Storage, and Homogenization.

characterized by overall low concentration and/or low interconnectivity of interstitial fluids. The FHRZ is roughly located at a distance of 100–200 km from the trench, a region where petrological models predict that low amounts of fluids are released from dehydration of the slab in cold subduction environments such the Central Andes (e.g., Hyndman & Peacock, 2003).

The upper crustal LRZs found in the forearc (C1, P1, and P2) roughly coincide with areas where major trench-parallel faults systems intersect transverse faults. The intersection of these faults system may facilitate the creation of pull apart basins under transtensional settings (e.g., Richards et al., 2001). Basins with thick Cenozoic sedimentary infill have been inferred below areas where the COT transverse fault intersects the Coastal Cordillera (Salar Grande, e.g., Reijs & McClay, 1998) or the Precordillera (Calama Basin, e.g., Jordan et al., 2010; see Figure 6a). C1 is located below the northern segment of the Salar Grande basin, an area which exhibits active crustal seismicity (Bloch et al., 2014) and has been interpreted as loci of recurrent deformation at least since the Oligocene (González et al., 2003; Reijs & McClay, 1998). P1 and P2 are centered roughly where the Precordillera Fault system is intersected by the COT and the Lípez-Coranzuli (LC) transverse faults, respectively (see Figure 6a). P1 corresponds with clusters of crustal seismicity reported in Bloch et al. (2014) below the Precordillera at ~21°S. We interpret that forearc LRZs may represent accumulation and circulation of fluids in crustal areas characterized by high permeability and low strength.

5.2. Structure of the Arc and Backarc Regions and Implications for Magmatism

Our preferred model shows a number of LRZs below the Western Cordillera at different depths (region W in Figure 4), suggesting a complex distribution of magma/fluid reservoirs below the active volcanic arc. Below the Pica volcanic gap (~20°–20.5°S), the model shows that the entire continental crust is dominated by high resistivities (>1,000 Ωm, see Figures 5a and 6), although a deep LRZ (P3 in Figure 5a) should indicate the availability of fluids or partial melts in the forearc mantle. The high resistivities suggest that the continental crust below the Pica gap represents a block of anomalously low permeability, which precludes the upward circulation and storage of fluids accumulated in the mantle, inhibiting the development of active volcanism below this segment of the Western Cordillera.

Between 20.5° and 23°S, our model shows that resistivities <30 Ωm predominate below the Western Cordillera. This resistivity domain roughly coincides with the western margin of the APVC (see Figures 4 and 6). The largest LRZ below the Western Cordillera is a ~150-km-long feature located mostly at 50- to 80-km depth (W1 and W2, see Figures 4c and 4d, 5b–5d, and 6b and 6c), which partially coincides with zones of high seismic attenuation (Schurr et al., 2003; Figures 5d, 6b, and 6c). We interpret this feature as a huge concentration of partial melts in the lower crust, which probably extends below the continental Moho, likely representing a Melting, Assimilation, Storage, and Homogenization zone usually proposed at the roots of subduction zone magmatism (e.g., Hilderth & Moorbath, 1988). W2 coincides with a segment of intraslab intermediate-depth seismicity where recorded earthquakes are concentrated below the Western Cordillera at 80- to 150-km depth (Figures 5c, 5d, and 6c). We speculate that both the concentration of intermediate-depth seismicity and the location of W2 are indicating that relatively higher amounts of fluids are released from the slab at this segment of the subduction zone, as Sippl et al. (2018) suggested to explain the distribution of seismicity in the forearc. Higher amounts of fluids released from the slab should result in larger generation of intraslab intermediate-depth earthquakes assuming dehydration embrittlement (see e.g., Hacker et al., 2003), and in larger degree of partial melting of the forearc mantle. Additional LRZs are observed below the active volcanic chain at 5- to 20-km depth (e.g., LRZ at <10-km depth below San Pedro and Azufre volcanoes in Figure 5c). We interpret these features as small magma chambers and/or hydrothermal fluid reservoirs emplaced at different levels of the middle and upper crust, representing varying stages of the subduction plumbing system.

The continental crust below the Western Cordillera shows high resistivities (>1,000 Ω) south of 23°S (see Figures 4 and 5e). In this region, Götze and Krause (2002) interpreted a high-density block between 10- and 38-km depths to explain the presence of a crustal-scale gravity anomaly (the Central Andean gravity high, CAGH). It has been suggested that this block represents a low-permeability and high-strength region of the crust, which explains why records of deformation, magmatism, and large hydrothermal systems are concentrated along the margins of the CAGH (e.g., Götze & Krause, 2002; Schurr & Rietbrock, 2004; Yáñez et al., 2008). The presence of a low-permeability block is consistent with high resistivities observed in our model along the CAGH (Figures 5e and 6b). Based on the composition and geochemical signature of basaltic lavas found in this segment of the arc, previous work has suggested that eruptive centers are fed by primitive magmas derived from melting of the mantle with low crustal contamination (e.g., Matteini et al., 2002; van Alderwerelt, 2017). These magma characteristics and high resistivities obtained by our model suggest that large volumes of partial melts are absent in this segment of the continental crust (Figure 7c). Schurr et al. (2003) interpreted that volcanism in this region may be fed by magma reservoirs located in the backarc region, to explain the distribution of high seismic attenuation zones that seem to connect the arc magmatism and the cluster of intraslab seismicity at 200-km depth (see NE-SW-oriented seismic cluster in Figure 7a). This hypothesis seems to be consistent with the presence of A2 in our preferred model and a couple of shallower LRZs that we found in the backarc (Figures 5e and 7c). However, we cannot discard the presence of magma reservoirs located below the arc but at depths exceeding 60 km, where our model seems to have low resolution (Figure 5e).

5.3. Variability in the Fluid Content of the Forearc Mantle

Between 20° and 23°S, the forearc mantle exhibits three LRZs (P3–P5), which roughly coincide with zones of high *Vp*/*Vs* ratio shown in Comte et al. (2016; see Figures 5a–5d). Low resistivities (<5 Ωm) and high Vp/Vs ratio in the forearc mantle wedge can be attributed to fluids produced by serpentinization of the mantle (Reynard et al., 2011). The intraslab intermediate-depth seismogenic zone show scattered and relatively

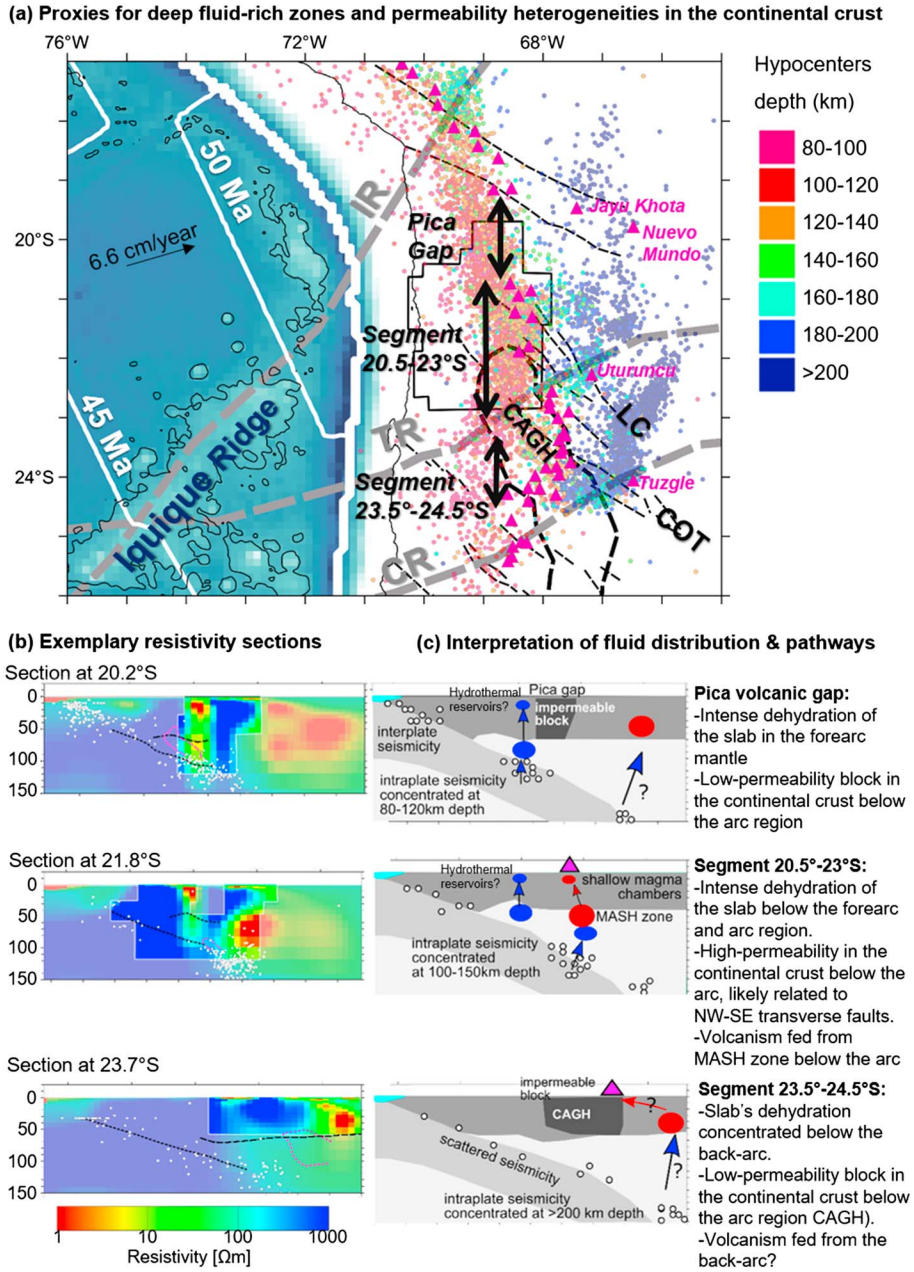

Figure 7. Interpretation of factors controlling segmentation of fluid processes along the study area. (a) Map with proxies for fluid-rich zones within the oceanic slab and mantle wedge and for permeability heterogeneities in the continental crust. Black thin line in the seaside is the bathymetry contour of 4,000 km below sea level, which roughly outlines the Iquique Ridge (proxy for a possible fluid-rich zone within the slab). White lines indicate isochrons of the Nazca plate (Müller et al., 1997). Gray dashed lines are hotspot tracks taken from Bello-González et al. (2018): CR = Copiapó Ridge/Caldera Hotspot; IR = Iquique Ridge/Foundation Hotspot; TR = Taltal Ridge/San Félix Hotspot. Colored dots are hypocenters for events located between 80- and ~300-km depths (intermediate-depth seismicity, proxy for slab's dehydration). Black dashed thin lines are NW-SE transverse faults taken from Richards et al. (2001) and Tibaldi et al. (2009; proxies for highly permeable zones). Black thick line encloses the location of the CAGH gravity anomaly taken from Götze and Krause (2002; proxy for a zone of low permeability). Pink triangles indicate active volcanoes. Black thin polygon in the continental side shows the area of the model with good resolution at depths >57 km. (b) Exemplary depth sections across our resistivity model representing the three major domains interpreted. (c) Cartoon illustrating major fluid pathways and reservoirs interpreted in the three domains. CAGH = Central Andean gravity high; LC = Lípez-Coranzuli; COT = Calama-Olacapato-El Toro; MASH = Melting, Assimilation, Storage, and Homogenization.

lower concentration of seismicity at 70- to 150-km depth between 23° and 24°S (see Figures 5e and 6c). If intraslab intermediate-depth earthquakes were caused by dehydration embrittlement processes (e.g., Hacker et al., 2003), such decrease in seismicity would indicate lower amount of fluids released by eclogitization of the slab. A reduction in the volume of fluids released from the slab is consistent with the relatively higher resistivities suggested by our model and MT data in this segment of the forearc mantle wedge (see Sensitivity Tests 7 and 8 in the supporting information), although resolution tests show that the inverted data set has low resolution in this region. We interpret, therefore, that seismological data and our model likely indicate that the amount of fluids in the forearc mantle tend to decrease between 23° and 24°S.

5.4. Factors Controlling the Distribution of Fluids in Subduction Zones

The complex distribution of LRZs in our resistivity model indicates significant variability in the crustal-scale distribution of fluids in the Central Andes subduction zone. To explain the distribution of LRZs (~fluid rich zones) in the study area, we compared their spatial distribution with proxies for factors that may control the generation, transport and storage of fluids within subduction zones. Figure 7a shows geophysical features we interpret as proxies for: (i) the amount of fluids carried by the oceanic slab (seamounts), (ii) the amount of fluids released by the slab dehydration (intermediate-depth seismicity), and (iii) the presence of high- and low-permeability structures within the continental crust (major transverse faults and the CAGH). We observe that both deep sources of fluids and factors likely facilitating/impeding the migration of fluids through the continental crust exhibit significant variability over the study area (Figure 7a). We suggest that a complex interplay between sources for deep fluids and permeability of the crust may determine the segmentation inferred in the fluid distribution (Figure 7c).

Factors controlling the amount of fluids released by dehydration reactions are the amount of fluids stored in the slab and/or the prevailing thermodynamic conditions of the slab at a particular depth. It has been suggested that age and thermal state of the slab play a key role in the amount of fluids released in the forearc region (e.g., Völker & Stipp, 2015). Isochrones of the ocean floor (Müller et al., 1997) show that the age of the Nazca plate, at least along the trench, does not significantly vary in our study area (Figure 7a). Dehydration of the slab is also controlled by thermodynamic conditions (e.g., Peacock, 1990), and therefore, relative variations in the depth of the oceanic plate or in the thermal structure of the mantle can be relevant. However, geophysical and thermomechanical models suggest that both depth and temperature of the slab vary smoothly along-margin within the study area (e.g., Ji et al., 2018; Sippl et al., 2018). A remaining factor to explain our observations is along-margin variability in the hydration of the oceanic plate, which can be enhanced with the subduction of seamounts and with presence of pervasive fault systems within the slab (e.g., Pommier & Evans, 2017; Ranero et al., 2005). Previous studies have suggested that the hydration of the slab in the study area increases with subduction of the Iquique Ridge, based on north-south variations observed in Vp/Vs ratio and seismicity in the forearc (Comte et al., 2016; Contreras-Reyes & Carrizo, 2011; Sippl et al., 2018). Figure 7 shows that NE-SW trending clusters of intraslab seismicity observed at depths >200 km in the backarc roughly coincides with the interpreted subducted tracks of the Taltal and Copiapó ridges (Bello-González et al., 2018; see gray dashed lines and dark blue dots in Figure 7a). We cannot rule out, therefore, that already subducted seamounts may also contribute to explain variability in the slab's hydration.

Fluids in the continental crust seem to concentrate close to areas where trench-parallel faults intersect transverse faults. The intersection of major fault systems may represent areas of high permeability and low strength in the lithosphere (e.g., Richards et al., 2001). Such permeable and weak areas can explain the correlation between LRZs and clusters of crustal seismicity observed in the forearc (e.g., below the Salar Grande and the Precordillera at ~21°S). Prior work suggested that transverse faults such as the COT have played a key role controlling the distribution of magmatism and hydrothermal fluid flow in the arc and backarc region of the Central Andes (e.g., Acocella et al., 2011; Chernicoff et al., 2002; Mazzuoli et al., 2008; Richards et al., 2001; Yáñez et al., 2008). Figure 7a shows that active volcanoes between 20.5° and 23.5°S are located in areas where transverse NW-SE faults cross above clusters of intraslab intermediate-depth seismicity. Active volcanoes are also found in the backarc where NW-SE transverse faults coincide with clusters of intermediate-depth seismicity at depths >200 km (e.g., Uturuncu and Tuzgle volcanoes in Figure 7a). Conversely, major transverse faults seem to be absent in the Pica gap (see ~19°–20.5°S in Figure 7a). The presence of LRZs in the forearc mantle above clusters of intraslab intermediate-depth seismicity suggest that

significant amounts of fluids are released from the slab below the Pica gap (Figures 6a and 7a). However, high resistivities dominating the continental crust (Figure 5a) and the lack of active volcanoes indicate that large magma reservoirs are absent below this segment of the arc. We speculate that this part of the Western Cordillera represents a block with anomalously low permeability, which precludes circulation of magmas or fluids within the continental crust (Figure 7c). Existing fluids/magmas at the base of the crust may be forced to migrate to regions of the forearc or backarc (Figure 7c).

The resistivity model shows the presence of LRZs along the Precordillera region at different depth levels, from the forearc mantle wedge to the upper crust (see, e.g., Figures 5a and 5b). A number of MT studies in other subduction zones have observed LRZs in the forearc mantle, which are often interpreted as accumulation of fluids released by serpentinization of the mantle (e.g., Reynard et al., 2011). In our study area, the distribution of seismicity (Bloch et al., 2014) and seismic reflectivity anomalies (Yoon et al., 2009) suggest the presence of fluid pathways connecting the forearc mantle LRZs with upper levels of the crust in the Precordillera at ~21°S (see P4 and dark pink polygon in Figure 5b). Seismic and resistivity features indicate, therefore, that fluids from the mantle may also ascend into the overriding plate at some permeable regions of the forearc (Figure 7c). It remains elusive if those fluids feed the LRZs observed at upper crustal levels in the forearc (e.g., P1 and P2 in our study area).

6. Conclusions

Based on 3-D inversion of long-period MT data collected at 56 sites located between 20°S and 24°S, we derived the lithospheric-scale resistivity structure of the subduction zone along the Central Andes. We found a meaningful model by joint inversion of MT impedances and vertical magnetic transfer functions in a period range of 10–10,000 s. Our model's responses show good data fit, reproducing all major trends in the observations. Sensitivity tests confirmed robustness of major resistivity features obtained in the forearc and arc regions.

Our resistivity model is consistent with major lithospheric structures described by other geological and geophysical studies. The most prominent structure of the model is a high resistivity zone (the forearc high resistivity zone, FHRZ, >1,000 Ωm) that dominates the forearc approximately between the coastline and the Precordillera. The FHRZ coincides spatially with dense, rigid, and cold crustal regions, as suggested by gravimetric, seismic, and thermal studies. We interpret the FHRZ as a low-permeability block, located over a segment of the forearc where low amounts of fluids it is expected to be released from the subducted slab.

The MT inversion model reveals an overall complex 3-D resistivity structure with several crustal-scale LRZs at various depth ranges and segments of the continental crust and mantle:

- In the continental forearc, most of LRZs are found in the upper and lower crust of the Precordillera region. The center of these LRZs are located closed to areas where major trench-parallel fault systems intersect with transverse faults (e.g., COT). Most of these LRZs coincide spatially with zones of active seismicity.
- Three major domains can be distinguished along the arc in north-south direction. The region of the Pica volcanic gap (~20°–20.5°S) is characterized by high resistivities (>1,000 Ωm) within the entire continental crust. Between 20.5° and 23°S, the arc exhibits several LRZs at different levels of the continental crust, including a ~150-km-long LRZ located in the lower crust and upper mantle, which may be evidence of a huge Melting, Assimilation, Storage, and Homogenization zone. Between 23° and 24°S, the resistivity structure below the volcanic chain is dominated by high resistivities (>1,000 Ωm), suggesting the absence of large magma reservoirs in this segment of the continental crust.
- Large LRZs were obtained in two segments of the backarc domain: below the Altiplano region at 21°S and close to the eastern margin of active volcanoes located at 23°–24°S. Both LRZs seem to be large reservoirs of partial melts within the crust.
- The forearc mantle exhibits major LRZs between 20° and 23°S, in areas where seismic studies suggested relatively higher amount of fluids in the mantle and where intermediate-depth seismicity is concentrated below the forearc and arc regions at 80- to 150-km depth.

The spatial distribution of LRZs suggests that the lithospheric-scale fluid distribution in the Central Andes subduction zone is controlled by a complex interplay between hydration of the slab and permeability of the

continental crust. LRZs in the subcontinental mantle are located in the forearc mantle wedge and above clusters of intermediate-depth seismicity. These LRZs are likely related to fluids produced by serpentinization of the mantle and eclogitization of the slab. LRZs in the continental crust forearc were found in areas where trench-parallel faults intersect transverse faults. Forearc LRZs may represent accumulation and circulation of fluids through highly permeable domains of the crust.

Acknowledgments
Jaime Araya Vargas has been partly supported by FONDAP project 15090013 (Centro de Excelencia en Geotermia de los Andes, CEGA) and FONDECYT Postdoctoral Grant 3180182. The results presented in this paper rely on data collected with the IPOC array (www.ipoc-network.org) and during various experiments funded by the Deutsche Forschungsgemeinschaft (DFG). We thank these initiatives, the institutions supporting them, and all people that participated in the acquisition of the data here modeled. Jaime Araya Vargas gratefully acknowledges Gary Egbert and Anna Kelbert for providing the ModEM3d inversion code, the GeoForschungsZentrum (GFZ) Potsdam for facilitating its computational cluster to invert the data, the Geophysical Instrument Pool Potsdam (GIPP) for supplying part of the instrumentation, and Daniel Díaz for providing codes to convert different data formats. We thank the associate editor and an anonymous reviewer for their comments, which significantly contributed to improve the original version of this paper. Some figures were prepared using Quantum GIS. Data (MT transfer functions) may be requested by contacting Heinrich Brasse (heinrich.brasse@fu-berlin.de) and Oliver Ritter (oritter@gfz-potsdam.de).

References

Acocella, V., Gioncada, A., Omarini, R., Riller, U., Mazzuoli, R., & Vezzoli, L. (2011). Tectonomagmatic characteristics of the back-arc portion of the Calama–Olacapato–El Toro Fault Zone, Central Andes. *Tectonics*, *30*, TC3005. https://doi.org/10.1029/2010TC002854

Allmendinger, R., & González, G. (2010). Neogene to Quaternary tectonics of the Coastal Cordillera, northern Chile. *Tectonophysics*, *495*(1-2), 93–110. https://doi.org/10.1016/j.tecto.2009.04.019

Amilibia, A., Sàbat, F., McClay, K., Muñoz, J., Roca, E., & Chong, G. (2008). The role of inherited tectono-sedimentary architecture in the development of the central Andean mountain belt: Insights from the Cordillera de Domeyko. *Journal of Structural Geology*, *30*(12), 1520–1539. https://doi.org/10.1016/j.jsg.2008.08.005

ANCORP Working Group (2003). Seismic imaging of a convergent continental margin and plateau in the Central Andes (Andean Continental Research Project 1996 (ANCORP'96)). *Journal of Geophysical Research*, *108*(B7), 2328. https://doi.org/10.1029/2002JB001771

Angermann, D., Klotz, J., & Reigber, C. (1999). Space-geodetic estimation of the Nazca-South America Euler vector. *Earth and Planetary Science Letters*, *171*(3), 329–334. https://doi.org/10.1016/S0012-821X(99)00173-9

Barazangi, M., & Isacks, B. L. (1976). Spatial distribution of earthquakes and subduction of the Nazca plate beneath South America. *Geology*, *4*(11), 686–692. https://doi.org/10.1130/0091-7613(1976)4<686:SDOEAS>2.0.CO;2

Bello-González, J. P., Contreras-Reyes, E., & Arriagada, C. (2018). Predicted path for hotspot tracks off South America since Paleocene times: Tectonic implications of ridge-trench collision along the Andean margin. *Gondwana Research*, *64*, 216–234. https://doi.org/10.1016/j.gr.2018.07.008

Bloch, W., Kummerow, J., Salazar, P., Wigger, P., & Shapiro, S. (2014). High-resolution image of the north Chilean subduction zone: Seismicity, reflectivity and fluids. *Geophysical Journal International*, *197*(3), 1744–1749. https://doi.org/10.1093/gji/ggu084

Brasse, H., & Eydam, D. (2008). Electrical conductivity beneath the Bolivian Orocline and its relation to subduction processes at the South American continental margin. *Journal of Geophysical Research*, *113*, B07109. https://doi.org/10.1029/2007JB005142

Brasse, H., Lezaeta, P., Rath, V., Schwalenberg, K., Soyer, W., & Haak, V. (2002). The Bolivian Altiplano conductivity anomaly. *Journal of Geophysical Research*, *107*(B5), 2096. https://doi.org/10.1029/2001JB000391

Burns, D. H., de Silva, S. L., Tepley, F. III, Schmitt, A. K., & Loewen, M. W. (2015). Recording the transition from flare-up to steady-state arc magmatism at the Purico-Chascon volcanic complex, northern Chile. *Earth and Planetary Science Letters*, *422*, 75–86. https://doi.org/10.1016/j.epsl.2015.04.002

Caldwell, T. G., Bibby, H. M., & Brown, C. (2004). The magnetotelluric phase tensor. *Geophysical Journal International*, *158*(2), 457–469. https://doi.org/10.1111/j.1365-246X.2004.02281.x

Chave, A. D., & Jones, A. G. (2012). *The magnetotelluric method: Theory and practice*. New York: Cambridge University Press. https://doi.org/10.1017/CBO9781139020138

Chernicoff, C. J., Richards, J. P., & Zappettini, E. O. (2002). Crustal lineament control on magmatism and mineralization in northwestern Argentina: Geological, geophysical, and remote sensing evidence. *Ore Geology Reviews*, *21*(3–4), 127–155. https://doi.org/10.1016/S0169-1368(02)00087-2

Chmielowski, J., Zandt, G., & Haberland, C. (1999). The Central Andean Altiplano-Puna magma body. *Geophysical Research Letters*, *26*(6), 783–786. https://doi.org/10.1029/1999GL900078

Coira, B., Davidson, J., Mpodozis, C., & Ramos, V. (1982). Tectonic and magmatic evolution of the Andes of northern Argentina and Chile. *Earth-Science Reviews*, *18*(3-4), 303–332. https://doi.org/10.1016/0012-8252(82)90042-3

Coira, B., & Kay, S. M. (1993). Implications of Quaternary volcanism at Cerro Tuzgle for crustal and mantle evolution of the Puna Plateau, Central Andes, Argentina. *Contributions to Mineralogy and Petrology*, *113*(1), 40–58. https://doi.org/10.1007/BF00320830

Comeau, M. J., Unsworth, M. J., Ticona, F., & Sunagua, M. (2015). Magnetotelluric images of magma distribution beneath volcán Uturuncu, Bolivia: Implications for magma dynamics. *Geology*, *43*(3), 243–246. https://doi.org/10.1130/G36258.1

Comte, D., Carrizo, D., Roecker, S., Ortega-Culaciati, F., & Peyrat, S. (2016). Three-dimensional elastic wave speeds in the northern Chile subduction zone: Variations in hydration in the supraslab mantle. *Geophysical Journal International*, *207*(2), 1080–1105. https://doi.org/10.1093/gji/ggw318

Contreras-Reyes, E., & Carrizo, D. (2011). Control of high oceanic features and subduction channel on earthquake ruptures along the Chile-Peru subduction zone. *Physics of the Earth and Planetary Interiors*, *186*(1-2), 49–58. https://doi.org/10.1016/j.pepi.2011.03.002

de Paolo, D. J. (1981). Trace element and isotopic effects of combined wallrock assimilation and fractional crystallization. *Earth and Planetary Science Letters*, *53*(2), 189–202.

de Silva, S. L. (1989). Altiplano-Puna volcanic complex of the Central Andes. *Geology*, *17*(12), 1102–1106. https://doi.org/10.1130/0091-7613

de Silva, S. L., & Kay, S. M. (2018). Turning up the heat: High-flux magmatism in the Central Andes. *Elements*, *14*(4), 245–250. https://doi.org/10.2138/gselements.14.4.245

Díaz, D., Brasse, H., & Ticona, F. (2012). Conductivity distribution beneath Lascar volcano (Northern Chile) and the Puna, inferred from magnetotelluric data. *Journal of Volcanology and Geothermal Research*, *217-218*, 21–29. https://doi.org/10.1016/j.jvolgeores.2011.12.007

Egbert, G. D., & Kelbert, A. (2012). Computational recipes for electromagnetic inverse problems. *Geophysical Journal International*, *189*(1), 251–267. https://doi.org/10.1111/j.1365-246X.2011.05347.x

Gardeweg, M. & Sellés, D. (2017). Characterization of the last volcanic products erupted in the Pica Gap (Northern Chile). *In* Actas XX Congreso Geológico Argentino, Sesión Técnica 7, 60–67.

Godoy, B., Wörner, G., Kojima, S., Aguilera, F., Simon, K., & Hartmann, G. (2014). Low-pressure evolution of arc magmas in thickened crust: The San Pedro-Linzor volcanic chain, Central Andes, Northern Chile. *Journal of South American Earth Sciences*, *52*, 24–42. https://doi.org/10.1016/j.jsames.2014.02.004

Godoy, B., Wörner, G., Le Roux, P., de Silva, S., Parada, M. A., Kojima, S., et al. (2017). Sr- and Nd- isotope variations along the Pleistocene San Pedro – Linzor volcanic chain, N. Chile: Tracking the influence of the upper crustal Altiplano-Puna Magma Body. *Journal of Volcanology and Geothermal Research*, *341*, 172–186. https://doi.org/10.1016/j.jvolgeores.2017.05.030

González, G., Cembrano, J., Carrizo, D., Macci, A., & Schneider, H. (2003). The link between forearc tectonics and pliocenequaternary deformation of the Coastal Cordillera, northern Chile. *Journal of South American Earth Sciences*, *16*(5), 321–342. https://doi.org/10.1016/S0895-9811(03)00100-7

Götze, H.-J., & Krause, S. (2002). The Central Andean gravity high, a relic of an old subduction complex? *Journal of South American Earth Sciences*, *14*(8), 799–811. https://doi.org/10.1016/S0895-9811(01)00077-3

Hacker, B. R., Peacock, S. M., Abers, G. A., & Holloway, S. D. (2003). Subduction factory 2. Are intermediate-depth earthquakes in subducting slabs linked to metamorphic dehydration reactions? *Journal of Geophysical Research*, *108*(B1), 2030. https://doi.org/10.1029/2001JB001129

Hayes, G. P., Wald, D. J., & Johnson, R. L. (2012). Slab1. 0: A three-dimensional model of global subduction zone geometries. *Journal of Geophysical Research*, *117*, B01302. https://doi.org/10.1029/2011JB008524

Hildreth, W., & Moorbath, S. (1988). Crustal contributions to arc magmatism in the Andes of Central Chile. *Contributions to Mineralogy and Petrology*, *98*(4), 455–489. https://doi.org/10.1007/BF00372365

Hyndman, R. D., & Peacock, S. M. (2003). Serpentinization of the forearc mantle. *Earth and Planetary Science Letters*, *212*(3-4), 417–432. https://doi.org/10.1016/S0012-821X(03)00263-2

Ji, Y., Yoshioka, S., Manea, V. C., Manea, M., & Suenaga, N. (2018). Subduction thermal structure, metamorphism and seismicity beneath north-central Chile. *Journal of Geodynamics*. https://doi.org/10.1016/j.jog.2018.09.004

Jordan, T., Nester, P., Blanco, N., Hoke, G., Dávila, F., & Tomlinson, A. (2010). Uplift of the Altiplano-Puna plateau: A view from the west. *Tectonics*, *29*, TC5007. https://doi.org/10.1029/2010TC002661

Kapinos, G., Montahaei, M., Meqbel, N., & Brasse, H. (2016). Three-dimensional electrical resistivity image of the South-Central Chilean subduction zone. *Tectonophysics*, *666*, 76–89. https://doi.org/10.1016/j.tecto.2015.10.016

Kelbert, A., Meqbel, N., Egbert, G. D., & Tandon, K. (2014). ModEM: A modular system for inversion of electromagnetic geophysical data. *Computers & Geosciences*, *66*, 40–53. https://doi.org/10.1016/j.cageo.2014.01.010

Kirby, S., Engdahl, R. E., & Denlinger, R. (1996). Intermediate-depth intraslab earthquakes and arc volcanism as physical expressions of crustal and uppermost mantle metamorphism in subducting slabs. In G. E. Bebout, et al. (Eds.), *Subduction top to bottom, Geophysical Monograph Series* (Vol. 96, pp. 195–214). Washington, DC: American Geophysical Union.

Koulakov, I., Sobolev, S. V., & Asch, G. (2006). P- and S-velocity images of the lithosphere-asthenosphere system in the Central Andes from local-source tomographic inversion. *Geophysical Journal International*, *167*(1), 106–126. https://doi.org/10.1111/j.1365-246X.2006.02949.x

Kühn, C., Küster, J., & Brasse, H. (2014). Three-dimensional inversion of magnetotelluric data from the Central Andean continental margin. *Earth, Planets and Space*, *66*(1), 112. https://doi.org/10.1186/1880-5981-66-112

Kukarina, E., West, M. E., Keyson, L. H., Koulakov, I., Tsibiov, L., & Smirnov, S. (2017). Focused magmatism beneath Uturuncu volcano: Insights from seismic tomography and deformation modeling. *Geosphere*, *13*(6), 1855–1866. https://doi.org/10.1130/GES01403.1

Lezaeta, P. (2001). Distortion analysis and 3-D modeling of magnetotelluric data in the Southern Central Andes. Doctoral dissertation, Freie Universität Berlin, Germany.

Matteini, M., Mazzuoli, R., Omarini, R., Cas, R., & Maas, R. (2002). Geodynamical evolution of Central Andes at 24°S as inferred by magma composition along the Calama–Olacapato–El Toro transversal volcanic belt. *Journal of Volcanology and Geothermal Research*, *118*(1–2), 205–228. https://doi.org/10.1016/S0377-0273(02)00257-3

Mazzuoli, R., Vezzoli, L., Omarini, R., Acocella, V., Gioncada, A., Matteini, M., et al. (2008). Miocene magmatism and tectonics of the easternmost sector of the Calama-Olacapato-El Toro fault system in Central Andes at ˜24°S: Insights into the evolution of the Eastern Cordillera. *Geological Society of America Bulletin*, *120*(11-12), 1493–1517. https://doi.org/10.1130/B26109.1

McGary, R. S., Evans, R. L., Wannamaker, P. E., Elsenbeck, J., & Rondenay, S. (2014). Pathway from subducting slab to surface for melt and fluids beneath Mount Rainier. *Nature*, *511*(7509), 338–340. https://doi.org/10.1038/nature13493

Meqbel, N. M., Egbert, G. D., Wannamaker, P. E., Kelbert, A., & Schultz, A. (2014). Deep electrical resistivity structure of the northwestern US derived from 3-D inversion of USArray magnetotelluric data. *Earth and Planetary Science Letters*, *402*, 290–304. https://doi.org/10.1016/j.epsl.2013.12.026

Meqbel, N. M. M. (2009). The electrical conductivity structure of the Dead Sea Basin derived from 2D and 3D inversion of magnetotelluric data. Doctoral dissertation, Freie Universität Berlin.

Müller, R. D., Roest, W. R., Royer, J.-Y., Gahagan, L. M., & Sclater, J. G. (1997). Digital isochrons of the world's ocean floor. *Journal of Geophysical Research*, *102*(B2), 3211–3214. https://doi.org/10.1029/96JB01781

Peacock, S. A. (1990). Fluid processes in subduction zones. *Science*, *248*(4953), 329–337. https://doi.org/10.1126/science.248.4953.329

Pommier, A., & Evans, R. L. (2017). Constraints on fluids in subduction zones from electromagnetic data. *Geosphere*, *13*(4), 1–16. https://doi.org/10.1130/GES01473.1

Pritchard, M. E., de Silva, S. L., Michelfelder, G., Zandt, G., McNutt, S. R., Gottsmann, J., et al. (2018). Synthesis: PLUTONS: Investigating the relationship between pluton growth and volcanism in the Central Andes. *Geosphere*, *14*(3), 954–982. https://doi.org/10.1130/GES01578.1

Ranero, C. R., Villaseñor, A., Phipps Morgan, J., & Weinrebe, W. (2005). Relationship between bend-faulting at trenches and intermediate-depth seismicity. *Geochemistry, Geophysics, Geosystems*, *6*, Q12002. https://doi.org/10.1029/2005GC000997

Reijs, J., & McClay, K. (1998). Salar Grande pull-apart basin, Atacama fault system, northern Chile. *Geological Society, London, Special Publications*, *135*(1), 127–141. https://doi.org/10.1144/GSL.SP.1998.135.01.09

Reutter, K. J., Scheuber, E., & Wigger, P. (Eds.) (1994). *Tectonics of the Southern Central Andes: Structure and evolution of an active continental margin*. Berlin, Heidelberg: Springer. https://doi.org/10.1007/978-3-642-77353-2

Reynard, B., Mibe, K., & Van de Moortèle, B. (2011). Electrical conductivity of the serpentinised mantle and fluid flow in subduction zones. *Earth and Planetary Science Letters*, *307*(3-4), 387–394. https://doi.org/10.1016/j.epsl.2011.05.013

Richards, J. P., Boyce, A. J., & Pringle, M. S. (2001). Geologic evolution of the Escondida area, Northern Chile: A model for spatial and temporal localization of porphyry Cu mineralization. *Economic Geology*, *96*(2), 271–305. https://doi.org/10.2113/gsecongeo.96.2.271

Salfity, J. (1985). Lineamentos transversales al rumbo andino en el noroeste Argentino. *4° Congreso Geológico Chileno*, volume 2.

Schaller, T., Andersen, J., Götze, H.-J., Koproch, N., Schmidt, S., Sobiesiak, M., & Splettstößer, S. (2015). Segmentation of the Andean margin by isostatic models and gradients. *Journal of South American Earth Sciences*, *59*, 69–85. https://doi.org/10.1016/j.jsames.2015.01.008

Schurr, B., Asch, G., Rietbrock, A., Trumbull, R., & Haberland, C. (2003). Complex patterns of fluid and melt transport in the central Andean subduction zone revealed by attenuation tomography. *Earth and Planetary Science Letters*, *215*(1-2), 105–119. https://doi.org/10.1016/S0012-821X(03)00441-2

Schurr, B., & Rietbrock, A. (2004). Deep seismic structure of the Atacama basin, northern Chile. *Geophysical Research Letters*, *31*, L12601. https://doi.org/10.1029/2004GL019796

Sernageomin (2003). Mapa Geológico de Chile escala 1:1.000.000. Servicio Nacional de Geología y Minería.

Sippl, C., Schurr, B., Asch, G., & Kummerow, J. (2018). Seismicity structure of the northern Chile forearc from >100,000 double-difference relocated hypocenters. *Journal of Geophysical Research: Solid Earth*, *123*, 4063–4087. https://doi.org/10.1002/2017JB015384

Sodoudi, F., Yuan, X., Asch, G., & Kind, R. (2011). High-resolution image of the geometry and thickness of the subducting Nazca lithosphere beneath northern Chile. *Journal of Geophysical Research*, *116*, B04302. https://doi.org/10.1029/2010JB007829

Soyer, W., & Brasse, H. (2001). A magneto-variation array study in the central Andes of N Chile and SW Bolivia. *Geophysical Research Letters*, *28*(15), 3023–3026. https://doi.org/10.1029/2000GL012095

Springer, M. (1999). Interpretation of heat-flow density in the Central Andes. *Tectonophysics*, *306*(3-4), 377–395. https://doi.org/10.1016/S0040-1951(99)00067-0

Stern, C. R. (2004). Active Andean volcanism: Its geologic and tectonic setting. *Revista Geologica de Chile*, *31*(2), 161–206.

Stern, R. J. (2002). Subduction zones. *Reviews of Geophysics*, *40*(4), 1012. https://doi.org/10.1029/2001RG000108

Tibaldi, A., Corazzato, C., & Rovida, A. (2009). Miocene–Quaternary structural evolution of the Uyuni–Atacama region, Andes of Chile and Bolivia. *Tectonophysics*, *471*(1-2), 114–135. https://doi.org/10.1016/j.tecto.2008.09.011

Unsworth, M., & Rondenay, S. (2013). Mapping the distribution of fluids in the crust and lithospheric mantle utilizing geophysical methods. In *Metasomatism and the chemical transformation of rock* (pp. 535–598). Berlin, Heidelberg: Springer.

van Alderwerelt, B. M. E. D. (2017). Diverse monogenetic volcanism across the main arc of the central Andes, northern Chile. Doctoral dissertation, University of Iowa.

Völker, D., & Stipp, M. (2015). Water input and water release from the subducting Nazca Plate along southern Central Chile (33 S-46 S). *Geochemistry, Geophysics, Geosystems*, *16*, 1825–1847. https://doi.org/10.1002/2015GC005766

Ward, K. M., Zandt, G., Beck, S. L., Christensen, D. H., & McFarlin, H. (2014). Seismic imaging of the magmatic underpinnings beneath the Altiplano-Puna volcanic complex from the joint inversion of surface wave dispersion and receiver functions. *Earth and Planetary Science Letters*, *404*, 43–53. https://doi.org/10.1016/j.epsl.2014.07.022

Wiese, H. (1962). Geomagnetische Tiefentellurik Teil II: Die Streichrichtung der Untergrundstrukturen des elektrischen Widerstandes, erschlossen aus geomagnetischen Variationen. *Geofisica Pura e Applicata*, *52*(1), 83–103. https://doi.org/10.1007/BF01996002

Wörner, G., Hammerschmidt, K., Henjes-Kunst, F., Lezaun, J., & Wilke, H. (2000). Geochronology (40Ar/39Ar, K-Ar and He-exposure ages) of Cenozoic magmatic rocks from northern Chile (18 22°S): Implications for magmatism and tectonic evolution of the central Andes. *Revista Geologica de Chile*, *27*(2), 205–240. https://doi.org/10.4067/S0716-02082000000200004

Wörner, G., Mamani, M., Ruprecht, P., Mercier, R., Hartman, G., Simon, K., & Thouret, J.C. (2003). Crustal control on central Andean magmatism in time and space: implications from geochemical data of igneous rocks between 16° and 27°S from Cretaceous to recent times. *X Congreso Geológico Chileno*, Concepción, Chile.

Wörner, G., Moorbath, S., & Harmon, R. S. (1992). Andean Cenozoic centers reflect basement isotopic domains. *Geology*, *20*(12), 1103–1106. https://doi.org/10.1130/0091-7613(1992)020<1103:ACVCRB>2.3.CO;2

Worzewski, T., Jegen, M., Kopp, H., Brasse, H., & Castillo, W. T. (2011). Magnetotelluric image of the fluid cycle in the Costa Rican subduction zone. *Nature Geoscience*, *4*(2), 108–111. https://doi.org/10.1038/NGEO1041

Yáñez, G., Rivera, O., Comte, D., Pardo, M., Baeza, L., & Vera, E. (2008). Damage zone and the occurrence of world-class porphyry copper deposits in the active margin of Chile: Geophysical signatures and tectonomagmatic inferences. International Symposium on Andean Geodynamics 7, 592–593.

Yoon, M., Buske, S., Shapiro, S., & Wigger, P. (2009). Reflection image spectroscopy across the Andean subduction zone. *Tectonophysics*, *472*(1-4), 51–61. https://doi.org/10.1016/j.tecto.2008.03.014

Yuan, X., Sobolev, S., Kind, R., Oncken, O., Bock, G., Asch, G., et al. (2000). Subduction and collision processes in the Central Andes constrained by converted seismic phases. *Nature*, *408*(6815), 958–961. https://doi.org/10.1038/35050073

References from the supporting information

Araya Vargas, J. (2016). Large-scale distribution of fluids in the subduction zone of Northern Chile—Constraints from magnetotelluric monitoring. Doctoral dissertation, Freie Universität Berlin.

de Silva, S., Zandt, G., Trumbull, R., Viramonte, J. G., Salas, G., & Jimenez, N. (2006). Large ignimbrite eruptions and volcano-tectonic depressions in the Central Andes: A thermomechanical perspective. *Geological Society of London, Special Publication*, *269*(1), 47–63. https://doi.org/10.1144/GSL.SP.2006.269.01.04

Díaz, D. (2011). Magnetotelluric study of the Western Cordillera (Northern Chile), with a focus on Lascar volcano. Doctoral dissertation, Freie Universität Berlin.

Egbert, G. D. (1997). Robust multiple-station magnetotelluric data processing. *Geophysical Journal International*, *130*(2), 475–496. https://doi.org/10.1111/j.1365-246X.1997.tb05663.x

Egbert, G. D., & Booker, J. R. (1986). Robust estimation of geomagnetic transfer functions. *Geophysical Journal of the Royal Astronomical Society*, *87*(1), 173–194. https://doi.org/10.1111/j.1365-246X.1986.tb04552.x

Haberland, C., Rietbrock, A., Schurr, B., & Brasse, H. (2003). Coincident anomalies of seismic attenuation and electrical resistivity beneath the southern Bolivian Altiplano plateau. *Geophysical Research Letters*, *30*(18), 1923. https://doi.org/10.1029/2003GL017492

Krings, T. (2007). The influence of robust statistics, remote reference, and horizontal magnetic transfer functions on data processing in magnetotellurics. Diploma thesis, Westfälische Wilhelms-Universität Münster.

Kühn, C., Brasse, H., & Schwarz, G. (2018). Three-dimensional electrical resistivity image of the volcanic arc in Northern Chile—An appraisal of early magnetotelluric data. *Pure and Applied Geophysics*, *175*(6), 2153–2165. https://doi.org/10.1007/s00024-017-1764-y

Ritter, O., Junge, A., & Dawes, G. J. (1998). New equipment and processing for magnetotelluric remote reference observations. *Geophysical Journal International*, *132*(3), 535–548. https://doi.org/10.1046/j.1365-246X.1998.00440.x

Schwarz, G., & Krüger, D. (1997). Resistivity cross section through the southern central Andes as inferred from magnetotelluric and geomagnetic deep soundings. *Journal of Geophysical Research*, *102*(B6), 11,957–11,978. https://doi.org/10.1029/96JB03626

Steveling, E. (1996). Erweiterung des aus MAGSON-Magnetometer und RAP-Datenlogger bestehenden Meßsystems. Protokoll zum 16. *Kolloquium Erdmagnetische Tiefensondierung*, Burg Ludwigstein.

Weckmann, U., Magunia, A., & Ritter, O. (2005). Effective noise separation for magnetotelluric single site data processing using a frequency domain selection scheme. *Geophysical Journal International*, *161*(3), 635–652. https://doi.org/10.1111/j.1365-246X.2005.02621.x